Characterization of an ettringite-based thermochemical energy storage material in an open-mode reactor

B. Chen, K. Johannes, M. Horgnies, V. Morin, F. Kuznik

Characterization of an ettringite-based thermochemical energy storage material in an open-mode reactor

B. Chen[1, 2], K. Johannes[1], M. Horgnies[2], V. Morin[2], F. Kuznik[1, *]

[1] *Université de Lyon, CNRS, INSA-Lyon, Université Claude Bernard Lyon 1, CETHIL UMR 5008, F-69621, Villeurbanne, France*

[2] *LafargeHolcim Innovation Center, 95 rue du Montmurier BP15, 38291 Saint Quentin Fallavier, France*

* Corresponding author. E-mail address: frederic.kuznik@insa-lyon.fr

Abstract

The mismatch between renewable energy supply and demand requires energy storage technologies to work out the dilemma. In thermal energy field, ettringite-based energy storage seems to be a good solution thanks to its high energy density and low material cost. It can store excess solar energy to meet the heating and domestic hot water demand in buildings. Therefore, the current work experimentally examines the energetic performance of an ettringite-based material made of commercial cements. The TG-DSC analysis shows the energy storage capacity of investigated material is as high as 282 kWh/m^3 original hydrated materials. Besides, the laboratory reactor tests prove the charging temperature is as low as 55–65 °C for ettringite. Under operating conditions, the average energy-releasing power during the full period is about 33.3 W/kg while the maximum power is about 915 W/kg original hydrated materials, which are significantly higher than most materials from the literature. The best volumetric energy-releasing density and the corresponding prototype storage density of the fixed-bed obtained are 176 kWh/m^3 original hydrated materials and 104 kWh/m^3, respectively.

Keywords: Ettringite-based material, Dehydration/hydration, Thermochemical energy storage, Fixed-bed reactor

Abbreviation

CSA	Calcium Sulfoaluminate
DA	Degree of advancement
DSC	Differential scanning calorimetry
OPC	Ordinary Portland cement
p-CAC	pre-blended Calcium Aluminate cement containing calcium sulphate
PWVP	Partial water vapor pressure [Pa]
RH	Relative humidity (%)
TCES	Thermochemical energy storage
TG	Thermogravimetry

Latin symbols

Cp	Specific heat capacity [J/(g·K)]
D	Diameter [cm]
E	Discharging energy quantity [J]
L	Length [cm]
m	Weight of sample [g]
$\dot{m}$	Mass flow rate [kg/h]
M	Molar mass [g/mol]
P	Power (W)
Q	Volumetric flow [m^3/h]
R	Ideal gas constant, 8.3145 J/(mol·K)

R^2	Determination coefficient
T	Temperature [°C]
W	Weight loss percentage (%)
X	Water molecule number
ΔH	Enthalpy [J/g]

Greek symbols

Δ	Difference
ϕ	Relative humidity [%]
ρ	Mass density [kg/m^3]

Subscripts

exp	Experiment
dry air	Dry air
H_2O	Water molecule
in	The entry of reactor
inlet	The inlet of system where the first thermos-hydrometer is
loss	Loss
mat.	Material
out	The exit of reactor
outlet	The outlet of system where the second thermos-hydrometer is
s	Sensible heat
sat	Saturated
st	Steam point
t	Time

V	Volumetric
w	Water
water vapor	Water vapor

30

1 Introduction

In EU-27, 79 % of final energy consumption in the residential sector is attributed to domestic hot water and space heating [1]. In contrast to this high demand, the excess solar heat in summer could not be used efficiently. Therefore, a solution is required in order to get rid of the seasonal mismatch of heating supply and demand. Throughout all possible technologies, the integration of thermochemical energy storage (TCES) systems into residential buildings is a promising solution, thanks to their low heat losses during the storage period and also high energy storage densities (about 100 – 500 kWh/m^3) [2].

Presently, numerous investigations about TCES materials have been done in microscopic tests and laboratory-scale experiments. The heat storage relies on a reversible chemical reaction, like oxide-hydroxide ($MgO/Mg(OH)_2$ [3] and $CaO/Ca(OH)_2$ [4–7]), oxide-carbonate ($CaO/CaCO_3$ [8]), reduction/oxidation ($(Mn_{0.75}Fe_{0.25})_2O_3/(Mn_{0.75}Fe_{0.25})_3O_4$ [9] and CoO/Co_3O_4 [10,11]), usually owe high energy densities but at high operating temperatures or pressures. Differently, the thermal energy storage by chemical sorption via salt hydrates could make the working temperatures lower than 150 °C in reactors: such concept is then adaptable to households.

Zondag et al. [12] reported a generated thermal power of 150 W (~ 139 kWh/m^3) in order to heat air from 50 to 64 °C by a 17 dm^3 of initial $MgCl_2 \cdot 6H_2O$ material in a packed bed open reactor system. Besides, they also indicated a loss of about 2/3 power to the exit airflow due to the inefficient heat recovery. Later, N'Tsoukpoe et al. [13] evaluated the suitability of 125 salt hydrates and concluded the most promising salt hydrates used for thermochemical energy storage are $MgSO_4 \cdot 7H_2O$, $SrBr_2 \cdot 6H_2O$, and $LaCl_3 \cdot 6H_2O$. Michel et al. [14] experimented with an open mode reactor with 400 kg of $SrBr_2 \cdot 6H_2O$ and obtained a high energy density of 203 kWh/m^3 with a storage capacity of 105 kWh. Zhao et al. [15] employed an $SrBr_2$ sorbent

composited of expanded natural graphite treated with sulfuric acid to store heat at 80 °C. The releasing thermal storage density was about 189 kWh/m^3 with a discharging power of 67.4 kW/m^3. In order to increase the permeability of packed bed, Hongois et al. [16] developed a $MgSO_4$ (15 wt%)-zeolite composite that possessed an energy density of 166 kWh/m^3 released at 25 °C in a packed bed reactor with 200 g of sorption material. All these reports give interesting and promising results of using salt hydrates to store thermal energy. However, the material cost of those solutions is still too high to be applied in residential buildings and individual houses [17]. The latest work from Courbon et al. [18] investigated the thermal performance of several high LiBr contents (32–53 wt%) composite materials (silica gel and activated carbon as holding matrix). Among them, the sample of 53 wt% LiBr being emerged in silica gel was improved most promising. Its theoretical energy storage density was 261 kWh/m^3 (dehydrated at 80 °C and energy released at 30 °C and 12.5 mbar water vapor pressure) while 160–175 kWh/m^3 in the open-mode set-up (at the level of 200 g) under similar experimental conditions. Moreover, a 58 wt% $SrBr_2$-silica gel composite was reported more performant than the LiBr composite [19]. Its energy storage density is as high as 203 kWh/m^3 in the reactor tests (dehydrated at 80 °C while hydrated at 30 °C and 12.5 mbar). Shkatulov et al. [20] used an encapsulating holding matrix material, mesoporous hollow silica spheres, to load salt hydrates ($LiCl{\cdot}H_2O$, $CaCl_2{\cdot}6H_2O$, $SrBr_2{\cdot}6H_2O$) for energy storage. Among the developed composites, the $CaCl_2$-based material presented the highest energy storage density of 222–278 kWh/m^3 with a temperature rise of 32 °C for a single cycle test in TGA/DSC. The storage capacity decreased to 139–208 kWh/m^3 for LiCl- and $SrBr_2$-based materials. Differently, Sun et al. [21] merged different contents (9–30 wt%) of LiCl into the microporous metal-organic framework (MOF, UiO-66) by wet impregnation method. The best thermal performance could be inferred as 900 kJ/kg, which equals to 200 kWh/m^3 with assuming the corresponding mass density of 800 kg/m^3 for 30 wt% LiCl-based composite.

Recent works [17,22] on the thermal properties of ettringite demonstrated a very good potential (material energy density ~ 500 kWh/m^3 with material cost inferior to 1000 €/m^3) to store low-temperature thermal energy resources (as low as 60 °C) by the reversible chemical reaction given in **Eq. 1**. The releasing of heat could be the corresponding reversible process by chemical sorption of liquid water or water vapor. In this reaction, $3CaO{\cdot}Al_2O_3{\cdot}3CaSO_4{\cdot}32H_2O$ is ettringite while $3CaO{\cdot}Al_2O_3{\cdot}3CaSO_4{\cdot}XH_2O$, with $X \neq 0$, is called meta-ettringite

$$3CaO \cdot Al_2O_3 \cdot 3CaSO_4 \cdot 32H_2O \overset{\Delta}{\leftrightarrow} 3CaO \cdot Al_2O_3 \cdot 3CaSO_4 \cdot XH_2O + (32 - X)H_2O\ (g)$$

(**Eq. 1**)

As to be a hydrated cement mineral phase, ettringite-based composite materials are more suitable for industrial production rather than synthesizing pure ettringite. Up to recently, all prototypes [23,24] using ettringite to store thermal energy were based on hydrated cement pastes containing high amounts of ettringite. Kaufmann and Winnefeld [24] used two mixtures of Calcium Sulfoaluminate (CSA) clinker and anhydrite to develop high ettringite contained materials (about 65 wt%). The energy storage density of rehydration by liquid water (pre-dehydrated at 110 °C) ranged from 60 to 70 kWh/m^3. These mixtures were then used in three different scale prototypes to: 1) rehydrate a block of 50 × 40 × 30 cm^3 by liquid water and raise the temperature from ~ 23 to 82 °C. 2) rehydrate 16 slabs of 50 × 10 × 3 cm^3 by humid air (90 % RH and 20 °C, 2 m/s) from ~ 24 to 37 °C; 3) use liquid water to hydrate 24 blocks (0.25 × 1 × 1 m^3) for 6 m^3 in a holiday house and a maximal increase of temperature up to 22 °C after 80 hours of manipulation. Ndiaye et al. [23] mixed 95 % CSA cement with 4 % lime and 1 % aluminum powder to prepare an aerated cement paste cylinder block of 68 % ettringite. The best energetic performance was 117 kWh/m^3 with 71 % of heat converted via water absorption by the cylindrical prototype (D16 × L32 cm). Compared to the

cases of [24], the energy-releasing density of ettringite composite material has been improved. However, the value is still very far from the theoretical energy density. Such difference can be explained by the use of liquid water requiring heat to change phase from liquid to vapor before reaction.

Despite the previous feasibility studies on the use of ettringite materials for thermal energy storage, the knowledge about the dehydration and hydration kinetics of ettringite-based materials is still lacking for microscale samples. In prototype surveys, the energy-releasing power and final energy storage density have not been able to find a compromise to meet the peak energy demand. Besides, aiming at reducing the material cost for future large-scale use, new ettringite-based materials shall be derived from commercial products manufactured by simple crafts. Therefore, the objective of this work is to develop a new low-cost ettringite-based material from a mixture of Ordinary Portland Cement (OPC) and pre-blended Calcium Aluminate Cement containing calcium sulfate (p-CAC). The material energy storage capacity and hydration/dehydration kinetics are characterized firstly by simultaneous thermal analysis of TG-DSC. In order to address daily use and to simplify the storage system, the macro energetic performance of the material is investigated in an open-mode reactor by operating conditions to reveal the real potential of the material.

2 Experimental method

2.1 Material preparation

A mixture (named C80P20) of Ordinary Portland Cement (20 wt%) and pre-blended Calcium Aluminate Cement (80 wt%) containing anhydrite was used to produce high ettringite content materials. The cement mixture was hydrated by demineralized water with high water to cement mixture ratio of 1.1. After 28 days of hydration, the content of ettringite was quantified by X-ray Powder Diffraction (XRD). The hardened paste of mixture furtherly

128 was milled down to 1 – 2 mm granules (Fig. 1). A few samples were stored in a plastic bottle
129 under the protection of soda-lime and silica gel for TG-DSC analysis. The rest was stored in
130 sealed plastic bags for later use.

131 

132 **Figure 1. Prepared ettringite-based granules of 1–2 mm.**

2.2 TG-DSC characterization

The prepared granules were ground down to powder inferior to 0.125 mm in diameter. The thermal characterizations for C80P20 powders were executed in the TG-DSC instrument under the control of water vapor content (Sensys Evo TG-DSC & Wetsys, Setaram Instrument). To dehydrate the samples, the temperature was rapidly increased to the setpoint with a heating rate of 10 K/min. The environment in the furnace was stabilized at the targeted humidity with an N_2 flow at 50 ml/min. After the removal of water, the dehydrated powder was cooled down to hydration temperature in pure N_2 flux. The dehydration conditions are detailed in Table 4. The hydration then carried out by regulating the Wetsys instrument (Setaram) for delivering a required humid N_2 flow. The hydration temperatures and humidity are detailed in Table 5. According to [25], the dehydration of ettringite at temperatures > 50 °C is a bivariant process while a mixture process of "monovariant" and "bivariant" for the rehydration of ettringite. Therefore, the degree of advancement (DA) for different processes is defined as:

$$\boldsymbol{DA = \frac{\Delta m_t}{m_{H2O,loss}}} \quad \textbf{(Eq. 2)}$$

Where Δm_t is the cumulative weight change at time t and $m_{H2O,\,loss}$ is the final weight loss of water for the dehydration in TG-DSC. It is worth noting that, powder sample was replaced by a new one after each experiment.

2.3 XRD analysis

The used XRD analysis was semi-quantitative. The instrument includes a Philips/PANalytical X'Pert Pro-MPD Powder Diffractometer and an X'Celerator detector of incident CuKα radiation beam (40 kV and 40 mA) to a rotation sample. The specimens were scanned from 2θ = [5–65 °] by a step of 0.25 °.

2.4 Mercury Intrusion Porosimetry (MIP)

Small pieces of hardened C80P20 pastes after 28 days of hydration were analyzed by MIP with using an Autopore IV (Micromeritics, USA). Before characterization, samples were oven-dried at 45 °C overnight. On this basis of a contact angle of 130 ° for ordinary cement pastes [26], the used pressures enabled a pore diameter coverage of about from 3 nm to 360 µm.

2.5 Reactor conception

Having considered the drawbacks of a closed system, the reactor is designed as an open-mode system with the circuit of ambient air (**Fig. 2a**). For storing energy (dehydration process), room air is pumped to the heat exchanger and heated up by the oil bath to a dehydration temperature similar to the one of heat source from solar collectors. The hot dry air flux is monitored by an anemometer and a thermo-hydrometer. The flux is then introduced into the reactor by the three-way valve once the set conditions are achieved. The temperatures of three different positions (the crosses in **Fig. 2b**) in the fixed bed are registered synchronously during all experiments by three thermal couples installed through the small hole in **Fig. 2c**. The small hole is plugged and sealed in order to avoid the leak of heat- and mass-carrier. Besides, two thermocouples are respectively installed at the entry and exit of the reactor to measure the fluid temperatures before and after passing through the fixed bed. The cylindrical reactor (**Fig. 2c**) and supporting nets (0.5 mm in hole size in **Fig. 2d**) is connected to the pipeline by double-pivot clamps. These amount of cylindrical reactors could be adapted to the weight of samples. In this study, one cylindrical reactor is used to load the materials. The end of desorption process is defined as that the relative humidity (RH) is identical in the upstream and downstream pipes. Contrarily, for discharging heat (hydration process), ambient air is firstly stabilized at the desired temperature with the mixture of water vapor supplied by

the vapor generator. After reaching the steady state, the humid air is imported into the reactor and hydrates anhydrous materials. The temperature evolution of the fixed bed is collected. Similar to the dehydration process, the difference of partial water vapor pressure (PWVP) is used to determine the reaction rate of progress. A picture of the reactor is given in **Fig. 2d**. For all tests, the reactor is insulated by 5 cm thick glass wool. The measurement ranges, as well as the uncertainty of the sensors, are detailed in **Tab. 1**. The time step of measurement is set to 2 s. The upside door of the isothermal room is closed to keep a constant temperature around the reactor during all experiments.

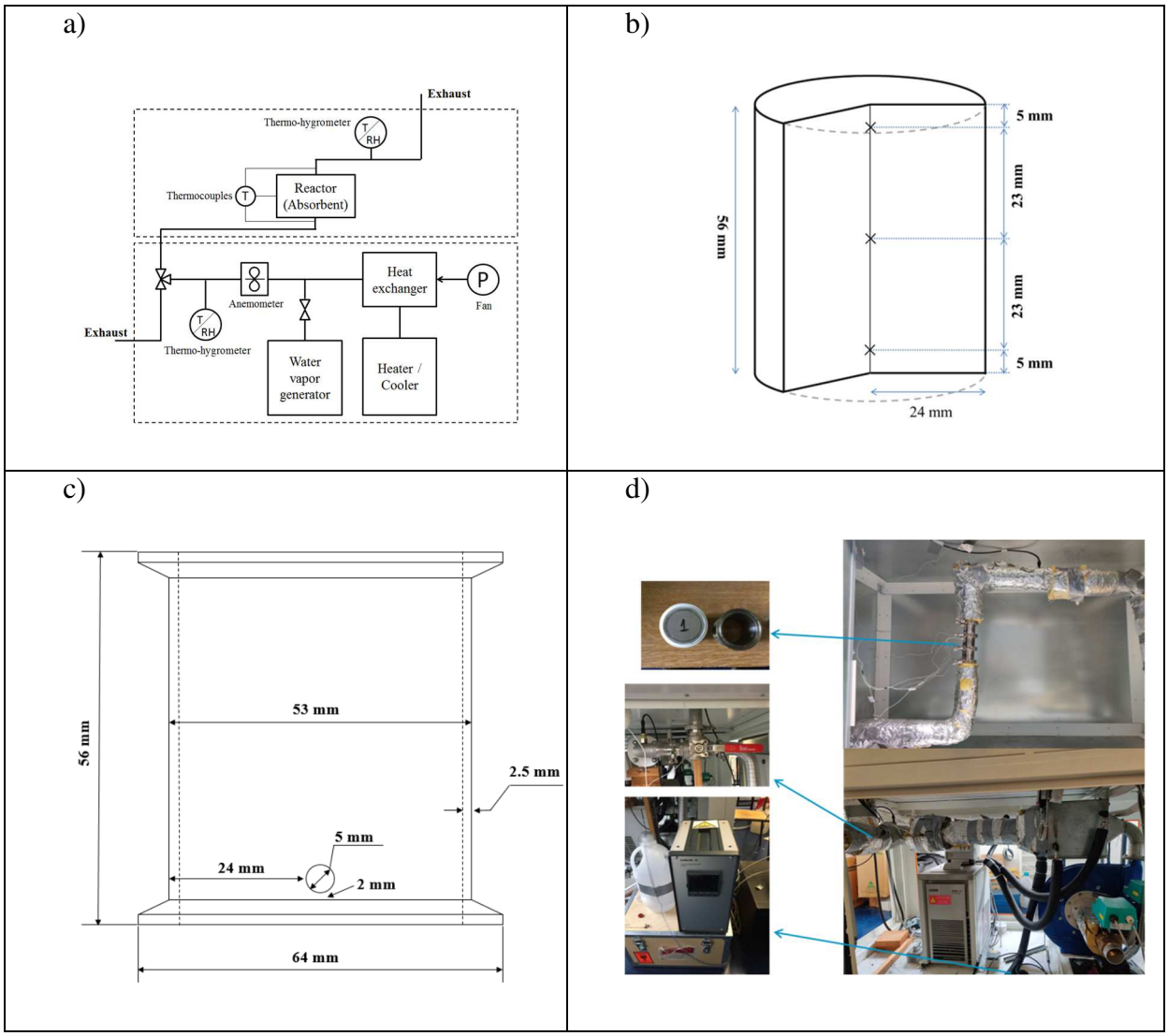

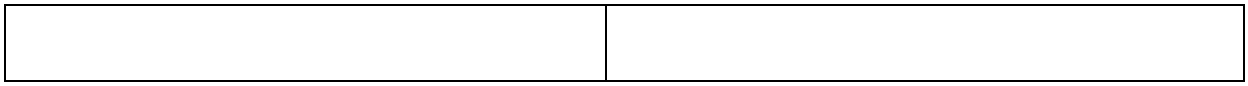

Figure 2. Reactor design: a) Schematic figure of reactor system, b) the positions of thermocouples in the fixed bed, c) Dimension of a reactor section and d) Picture of the prototype.

Table 1. Measurement range and uncertainty of the probes.

Probe	Measurement range	Uncertainty
Thermohygrometers (Rotronic, HygroClip type HC2-IC102)	-100 – 200 °C	± 0.1 °C
	0 – 95 % RH	± 0.8 % RH
Thermocouples (Type K)	0 – 100 °C	± 0.1 °C
Propeller anemometer (Schiltknecht, MiniAir20, steel)	40 m/s	1.5 % of measurement

2.6 Reactor test conditions

The kinetics of dehydration and hydration of the composite material is controlled by multi-parameters of the working fluid at the inlet of the reactor, such as temperature, humidity, and airflow. During each experiment, about 75 g of C80P20 grains filled the cylinder reactor. These granule samples were replaced by new ones after each experiment in order to minimize the lateral carbonation effects on ettringite [17,27]. For dehydration tests, the initial RH was not considered because the ambient water vapor content in the laboratory does not result in a significant difference in RH at high temperatures. An experimental design has been carried out on the de/hydration temperature, flowrate and RH. All the operating conditions are developed in **Tab. 2**. Dehydration temperatures have been set according to the outlet temperatures achievable by a classical solar air collector. After dehydration, the air flowrate is

turned off and the samples are cooled down by natural convection with the ambient environment. The door of the isothermal chamber is opened without unloading insulation. This step is important to mimic seasonal heat storage where charging sensible heat is lost. For hydration investigations, the temperature of the inlet humid air was pre-stabilized at 20 °C which is the set point temperature in a building during winter [2]. Besides, a comparison test of hydration at 15 °C is executed. The RH of fluid was controlled at around 90 % in various flowrates in order to facilitate the hydration process. The reactor flow rate is estimated by the scaling of a flow rate of 180 m^3/h and a daily storage by 2 – 3 kg material for an apartment of 100 m^2. The operating conditions of these hydration tests are summarized in **Tab. 2**. It is worth noting that the dehydration and hydration tests were carried independently with different granular samples.

Table 2. The operating conditions set for reactor tests.

Test numeration	Dehydration		Test numeration	Hydration		
	T [°C]	Flowrate [$m^3 \cdot h^{-1}$]		T [°C]	RH [%]	Flowrate [$m^3 \cdot h^{-1}$]
1	75	5.0	6	20	90	5
2	85	5.0	7	20	90	3
3	95	5.0	8	20	80	5
4	95	6.0	9	15	90	5
5	95	7.5	/	/	/	/

2.7 Data processing method

As shown in Fig. 2, the measuring devices during the reactor tests gave the following values:

- the RH of the fluid at the inlet ϕ_{inlet} and outlet ϕ_{outlet} of the system [%];
- the temperature of the moist air at the inlet T_{inlet} and the outlet T_{outlet} of the system [°C];
- the airflow rate Q_V in the system [$m^3 \cdot h^{-1}$];
- the temperature of the moist air entering the reactor T_{in} and exiting the reactor T_{out} of the system [°C];
- the temperatures at different positions in the reactor [°C]

The partial water vapor pressure, P [Pa], at the inlet and outlet of the system are calculated as:

$$P_{inlet,H2O} = P_{sat,T_{inlet}} \times \frac{\phi_{inlet}}{100\%} \textbf{(Eq. 3)}$$

$$P_{outlet,H2O} = P_{sat,T_{outlet}} \times \frac{\phi_{outlet}}{100\%} \textbf{ (Eq. 4)}$$

The saturated water vapor pressure $P_{sat,T}$ [hPa] at absolute air temperature T [K] can be drawn from Goff-Gratch equation [28]:

$$logP_{sat,T} = -7.90298\left(\frac{T_{st}}{T} - 1\right) + 5.02808\log\left(\frac{T_{st}}{T}\right) - 1.3816 \times 10^{-7}\left(10^{11.344\left(1-\frac{T}{T_{st}}\right)} - 1\right) + 8.1328 \times 10^{-3}\left(10^{-3.49149\left(\frac{T}{T_{st}}-1\right)} - 1\right) + logP_{st} \textbf{ (Eq. 5)}$$

where T_{st} is the steam-point of 373.15 K at 1 atm, P_{st} is the $P_{sat,T}$ at the steam-point pressure (1 atm = 1013.25 hPa)

The water absorption rate $\dot{m}_w$ is defined as the variation rate of water vapor content between the inlet $\dot{m}_{inlet}$ and outlet $\dot{m}_{outlet}$ in **Eq. 6**. R is the ideal gas constant equal to 8.3145 J/(mol·K). Thus, the quantity of absorbed water could be inferred by the integration of $\dot{m}_w$.

$$\dot{m}_w = \dot{m}_{inlet} - \dot{m}_{outlet} = \frac{P_{inlet,H2O} \cdot Q_V \cdot M_{H2O}}{R \cdot T_{inlet}} - \frac{P_{outlet,H2O} \cdot Q_V \cdot M_{H2O}}{R \cdot T_{outlet}} \quad \textbf{(Eq. 6)}$$

The usable system output power P_s [W] is estimated based on the sensible heat of air flow composed of dry air and water vapor:

$$P_s = Q_V \cdot \rho_{dry\ air} \cdot C_{p,dry\ air} \cdot (T_{out} - T_{in}) + \dot{m}_{outlet} \cdot C_{p,water\ vapor} \cdot T_{out} - \dot{m}_{inlet} \cdot C_{p,water\ vapor} \cdot T_{in} \quad \textbf{(Eq. 7)}$$

Where the specific heat capacity of air $C_{p,\ dry\ air}$ and of water vapor $C_{p,\ water\ vapor}$, dry air density $\rho_{dry\ air}$, molar mass of water vapor M_{H2O} and the variation of temperature ($T_{out} - T_{in}$) between the inlet and outlet of the reactor. It is worth noticing that all the enthalpies, energy densities and powers are calculated based on the mass of original hydrated materials (OHM, the granule samples of the hydrated cement mixture pastes without any de/re-hydration processes). The quantity of discharging energy E [J] is calculated as the following integral on the observation duration:

$$E = \int P_s \cdot dt \quad \textbf{(Eq. 8)}$$

3 Results and discussion

3.1 Ettringite content by XRD

After 28 days of hydration curing, some materials were collected and ground to powder (< 100 µm) for the semi-quantitative XRD analysis. The percentage was determined based on the strongest peak area and standard relative diffraction intensity for each mineral. Therefore, the ettringite content in the materials was then confirmed as 71.8 wt%. The rest trace phases are not presented in the Fig. 3 due to the very small patterns but are detailed in the Tab. 3. Note that: the components inferior to 1% could be neglected in this study.

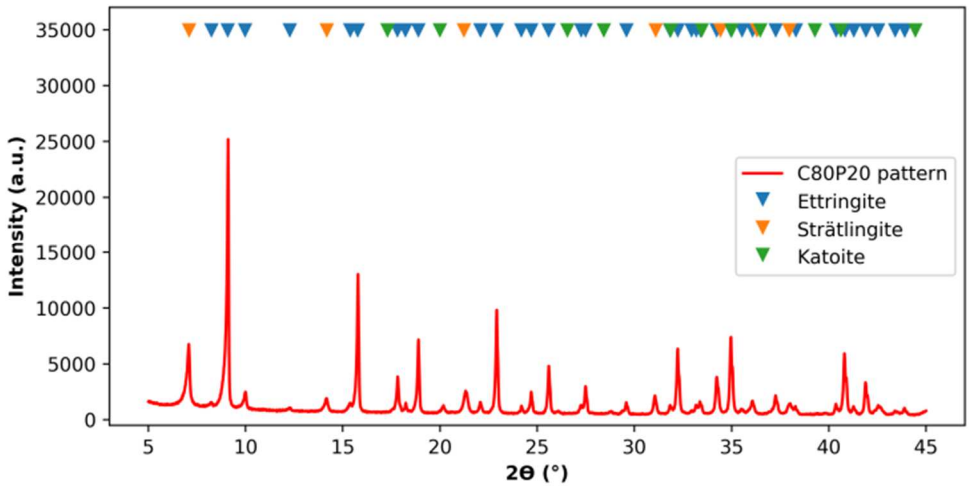

Figure 3. XRD analysis of C80P20 after hydration of 28 days.

Table 3. The content of different phases in C80P20.

Minerals	Content (wt%)
Ettringite	71.8
Strätlingite	25.1
Katoite	1.0
Alite	0.8

Larnite	0.5
Calcite	0.1
Aluminum hydroxide	0.7

3.2 MIP analysis

Seen from the Fig. 4, the cumulative pore volume of hydrated C80P20 is about 0.27 mL/g. After dehydrated at 90 °C for 2 days, the pore volume of each size increses and the cumulative volume is about 0.41 mL/g. The change of diameter for the pores in the C80P20 samples is shown in the figure below. After dehydration, the contraction of samples makes the size of big pores (around 1 μm) reduced. In terms of ettringite crystals, dehydration can lead to the reduction of crystal dimension [17] and a lot of small pores (< 0.1 μm) produced between meta-ettringite and holding structure. The material mass density is 1.25 g/cm^3 while 1.07 g/cm^3 after dehydration.

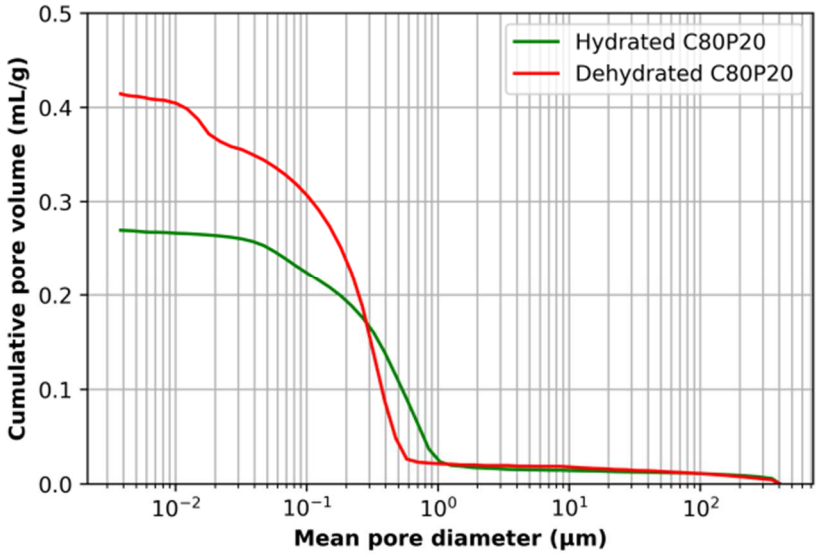

Figure 4. Pore volume of hydrated and dehydrated C80P20 samples.

3.3 TG-DSC analysis

3.3.1 *Dehydration analysis*

Dehydration tests have been carried out to study the influence of temperatures and PWVPs on the removal of water pore solution and structure water molecules. **Fig. 5** represents the kinetic results of different dehydration experiments. It is worth noting that, a new sample from the same series of sample preparation was used for each dehydration and hydration experiment. The degree of advancement is normalized by the respective total weight losses. The decreasing pressures of water vapor from 1200 to 400 Pa delivered into instruments in this study have a minor effect on the dehydration rates and the degree of water removal at 80 °C. The final water removed level stabilizes at 21.3 % for 800 and 1200 Pa while the value reaches 21.4 % for 400 Pa after 1.5 hours (see **Tab. 4**). The average endothermic energy is about 715 J/g OHM. In the case of dry N_2 only, the water loss reaches 25 % after 4 hours with an enthalpy of 811 J/g of hydrated materials. **Fig. 6** shows the tested equilibrium states of ettringite on the phase diagram. The dehydration points from 400 to 1200 Pa cluster near the thermo-equilibrium of the 9-hydrates meta-ettringite. For dry N_2 (treated as 0.01 Pa PWVP), the distance from the thermo-equilibrium increases the weight loss by 3.6 %. At 70°C, the material dehydration is more affected by the water vapor pressure. A higher PWVP decreases not only the dehydration rate but also the water loss level. Under the conditions of 800 Pa of PWVP and 60 °C it took 7 hours to dehydrate the sample by 16.5% whereas with temperature of 70 °C 20.3% was dehydrated within 2 hours. This lower weight loss trend as a function of temperature is caused by the approach of operating condition to the limit of ettringite dehydration. For the dehydration points, it can be assumed that there is a zone where the reaction is di-variant [29].

For a heterogeneous and stoichiometric water desorption [30], the variation of reaction enthalpy is as a linear function of the degree of reaction advancement (refers to the water loss

quantity in this study). Seen from Fig. 7, the endothermic energy during the process is linear with mass loss. The relative equation is assumed as $\Delta H = 30.321 \times W_{loss} + 58.788$ with the determination coefficient (R^2) of 0.962. It is worth mentioning that the slope of the linear curve corresponds to a reaction enthalpy of 54.6 kJ/mol_{water}, which is in good agreement with the value of other hydrated salts from the literature [30].

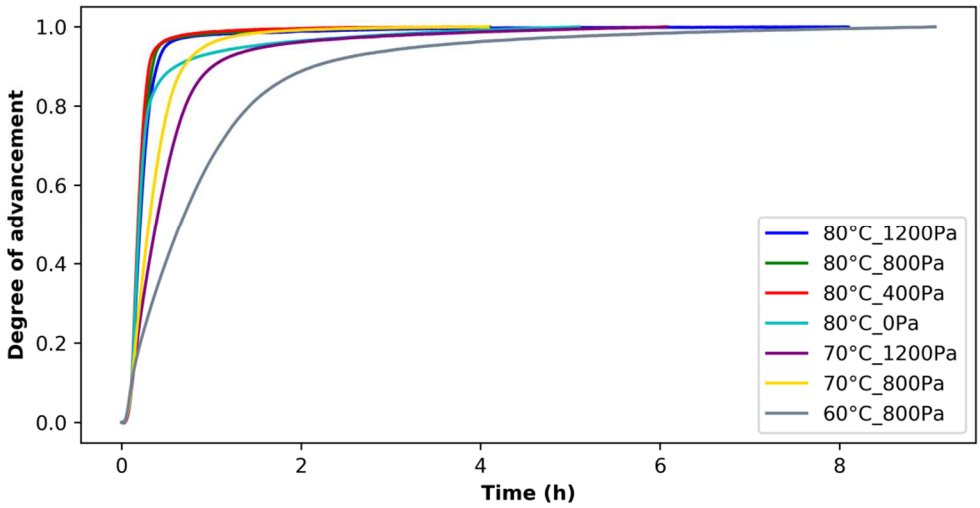

Figure 5. Dehydration of powder sample at various temperatures and PWVPs in the TG-DSC.

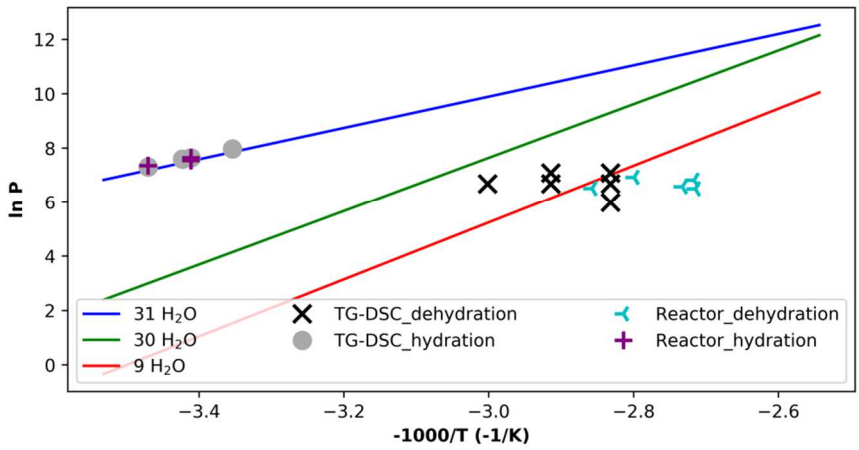

314 **Figure 6. Location of operating points in the de/hydration equilibrium curves of**

315 **ettringite.**

316

317 **Table 4. Dehydration results for C80P20 powders.**

Dehydration temperature (°C)	PWVP (Pa)	Final weight loss (%)	Number of water molecules loss per ettringite molecule	Enthalpy (J/g_{OHM})
80	1200	21.3	20.7	714
	800	21.3	20.7	703
	400	21.4	20.8	729
	0	25.0	24.3	811
70	1200	18.9	18.4	605
	800	20.3	19.7	667
60	800	16.5	16.0	570

318

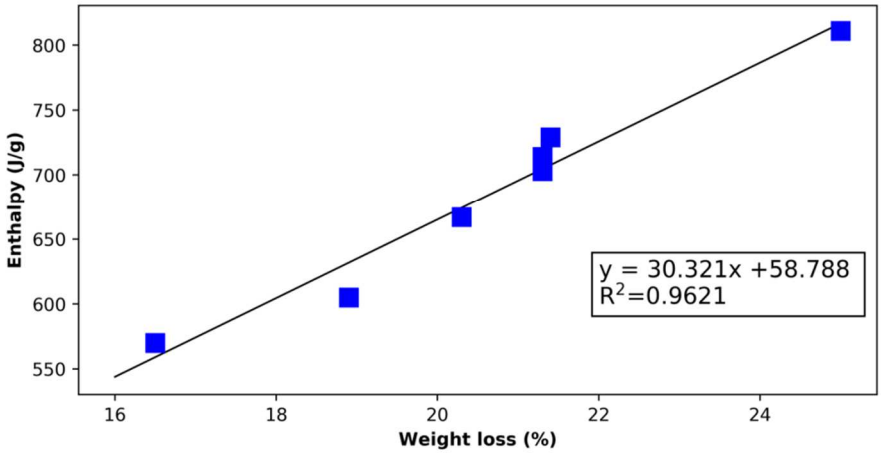

319

320 **Figure 7. Dehydration enthalpy as a function of the weight loss in TG-DSC.**

3.3.2 *Hydration analysis*

The dehydrated specimen was prepared at 80 °C under dry N_2 flow in TG-DSC. The hydration experiments were then carried out at about 90 % RH and for different temperatures. **Fig. 8** shows the DA and heat-releasing power for hydration at 20 °C at 2100 Pa (~ 90 % RH). The peaks observed on the heat flow curve allow separating the whole process into three stages. The first strong heat releasing process before 0.4 hours is with a DA of about 0.15. This step is probably due to a surface reaction that leads to a high reaction rate corresponding to a large slope given by the blue curve. Afterward, from 0.4 to 2.1 hours, the rate of water vapor sorption slows down and stabilizes. It leads to a nearly linear growth which is probably due to a steady diffusion of water vapor in the material grains. During this period, the discharging power gets firstly a slight rise to 0.18 mW and then decreases to 0.03 mW. The slow tendency of DA evolution in the last stage shows a quite slow water vapor sorption process. The heat-releasing power of this development is too small to be detected and the accuracy of signal is somehow influenced (waveform) between 3 to 17 hours. Therefore, the main accountable amount of heat is released during the first two stages. The quantity of water uptake in the sample is about 78 % of water removal weight during the preparation of the dehydrated sample. It is because the rehydration at late stage (after 3 hours) is very slow and the experiment is then stopped before the full hydration.

Fig. 9 shows the hydration curves of DA under the operating conditions given in **Tab. 5**. The set hydration temperatures ranging from 15 to 25 °C is under the consideration of using room air for rehydration. While a high RH could improve the process of rehydration. The three stages in the hydration at 20 °C are also observed in the other hydration experiments at 90 % RH. These stages could be distinguished by the DA: the first rapid sorption locates at 0 – 0.15, while the steady zone at 0.15 – 0. 55 and the final slow process at DA > 0.55. In **Tab.**

345 5, the hydration enthalpies at 15 and 20 °C are around 635 J/g of OHM with a DA of about
346 0.78. The enthalpy at 19 °C is slightly higher while the heat-releasing amount at 25 °C is
347 significantly higher. According to the Fick's diffusion law [31,32], a higher temperature leads
348 to a higher diffusion coefficient and the diffusion flux is monotonically proportional to water
349 vapor pressure. Therefore, the hydration rate at 25 °C has a higher sorption rate and amount of
350 water vapor. The higher added PWVP the faster the hydration. According to Fig. 6, the end
351 chemical state of reformed ettringite is a 31-hydrate if enough long time given. These final
352 hydration enthalpies are assumed to be equal to the heat quantity for removing water. It
353 should be noticed that the releasing heat is composed of the condensation heat of capillary
354 water and major chemical heat from ettringite hydration.

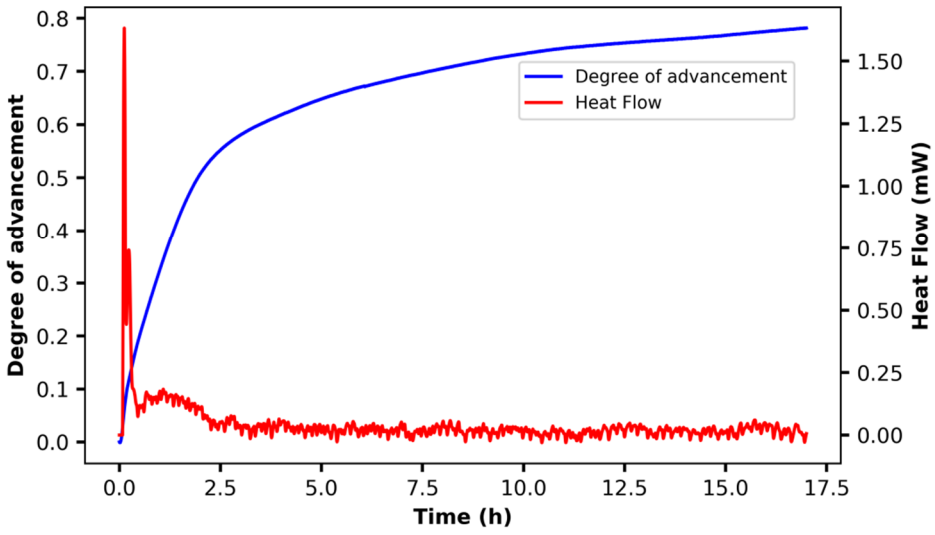

355

356 **Figure 8. Hydration kinetics of C80P20 powder sample at 20 °C & 2100 Pa.**

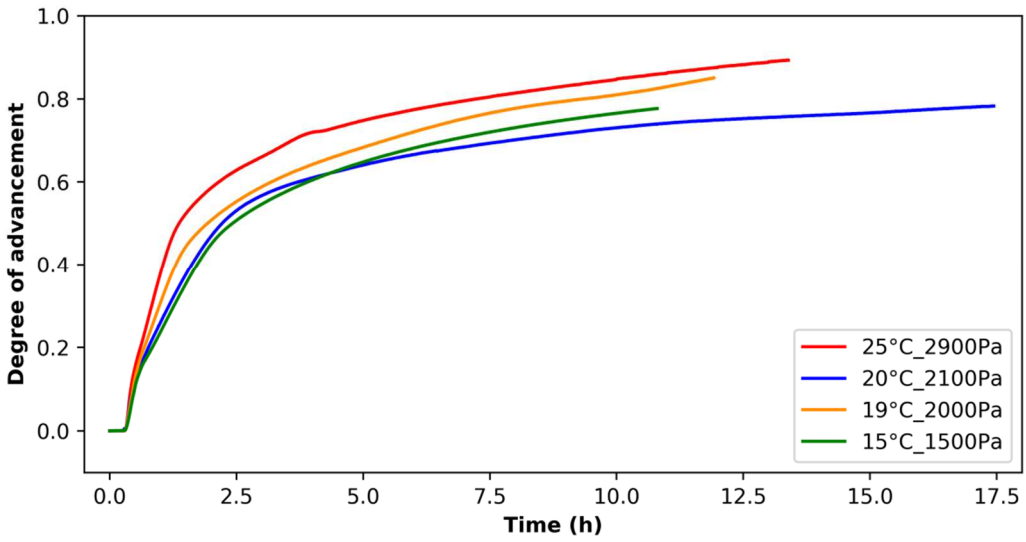

357

358 **Figure 9. Hydration under 90 % RH at various temperatures and PWVPs for**

359 **powder samples dehydrated at 80 °C & 0 Pa.**

360

361 **Table 5. Hydration results for C80P20 powders dehydrated at 80 °C & 0 Pa.**

Hydration temperature (°C)	PWVP (Pa)	RH (%)	Enthalpy (J/g $_{OHM}$) *
25	2900	91	755
20	2100	90	636
19	2000	91	652
15	1500	88	631

362 *The enthalpy is integrated by the baseline of 0 for the whole process even though the "Heat Flow"

363 signal is said imprecise in the third stage of hydration.

364 ### 3.4 Reactor tests for dehydration

365 The micro tests of kinetics were not enough to stand for de-/re-hydration processes at

366 reactor scale. Therefore, the reactor tests were supplemented. The water removal process was

367 started after the stabilization of dehydration conditions for the airflow (details are given in

368 section 2.4). Fig. 10 presents the dehydration experiment carried out for 95.2 °C and 6.1 m^3/h

(0.94 m/s). During the charging phase, the temperatures in the fixed bed gradually increased over time and were identical after 1 hour of heating. As being a porous material, the water removable in the grains is composed by water pore solution (physical desorption) and structural water in ettringite (chemical desorption).

The process of dehydration during the first 3 hours is specified in **Fig. 11**. Once the hot airflow introduced into the reactor, the bottom temperature increases steeply to 53.8 °C with a very strong release of water vapor up to about 2100 Pa. This quick growth of PWVP mainly comes from the evaporation of the pore solution in the materials. Later, the PWVP increases significantly to 2750 Pa until the temperature of the upper-position raises to 54.9 °C. Meanwhile, the temperature of the bottom material starts to rise again. The PWVP then falls to around 1400 Pa when the temperature of the whole fixed-bed climbs higher than 61.3 °C. Then, the pressure slightly increases to 1500 Pa and keep at almost the same level when the materials at the upper-position are heated. In this stage, the produced water vapor is supposed to be essentially coming from the dehydration of ettringite. Hereafter, the upper temperature reaches 88.3 °C as the bottom and middle temperature of the fixed-bed. The PWVP's decrease is delayed because some materials still need to be dehydrated at the top of the fixed-bed. These phenomena during heat storage are consistent with the three dehydration phases described by Pan and Zhao [33]. Besides, the studied operating conditions prove the possibility of using hot air from common solar air collectors to dehydrate ettringite materials in residential buildings.

It is worth noting that, at the second large increase of temperatures from 65.2 to 88.3 °C, the dehydration of ettringite is still occurring since a relatively high PWVP. However due to a more difficult process to remove the water molecules in the ettringite crystal structure than evaporation of pore solution, the slope of the curve is, at this stage, smaller than the one at the

first increase of temperature from 27.2 to 54.9 °C. When the temperatures of the whole fixed-bed approaches 90 °C, the last stage of dehydration is almost finished and the PWVP decreases significantly and forms a tail-off to finally stabilize at 600 Pa. These phenomena are similarly findable in the dehydration at different temperatures and airflow rates. The materials in the fixed-bed are completely charged by hot airflow when the PWVP at the outlet of the system is stable at the temperature of 95.2 °C.

Fig. 12 represents the variation of the difference between the temperatures of the entry and exit of the fixed-bed during the charging stage. The T_{in} raises very rapidly first of all while only a slight increase for the T_{out}. It results in the maximal temperature difference of 39.3 °C for the first stage. Then difference decreases down to 14.7 °C due to the increase of T_{out}. During this period, the temperature of the fixed bed ranged between 55–65°C. Afterward, the temperature difference increases to 20.9 °C for the second stage, with a duration approximately equal to three times the first stage one. Once the main dehydration of material is done, the airflow temperature at the outlet of reactor increases significantly, which leads to the second drop of temperature difference. However, the reactor is not totally adiabatic despite the use of thick glass wool insulation (~ 5 cm). The final temperature gap is about 0.6 °C between the two thermocouples (14.5 cm), which results in the heat loss power of 1.36 W according to **Eq. 7.** The temperature difference ΔT between the two positions is equivalent to 0.018 W/g of sample.

Tab. 6 summaries the dehydration experimental results. For dehydration at 95 °C, the average value of dehydration weight loss is 33.5 %. The small divergence may come from the different weight of samples loaded, which leads to some effect on bulk porosity and furtherly influences the dehydration procedure. Besides for similar sample mass, the lower the dehydration temperature the smaller the weight loss is. The weight losses in the reactor are

indeed bigger than in the TG-DSC analysis because of more pore solution in the non-silica gel dried reactor samples.

After the dehydration at 95 °C, the material is cooled down to ambient temperature with thermal insulation to simulate the temperature evolution in a real operating scenario, see in Fig. 10. It takes about 10 hours to discharge the sensible heat. Even though the temperatures of the materials decrease to ambient temperature (18.9 °C), the chemical energy is stored thanks to the dry condition in the reactor to avoid water re-adsorption. It is worth noticing that, after the dehydration, the contraction of granules can be observed due to the reduction of the height of fixed-bed.

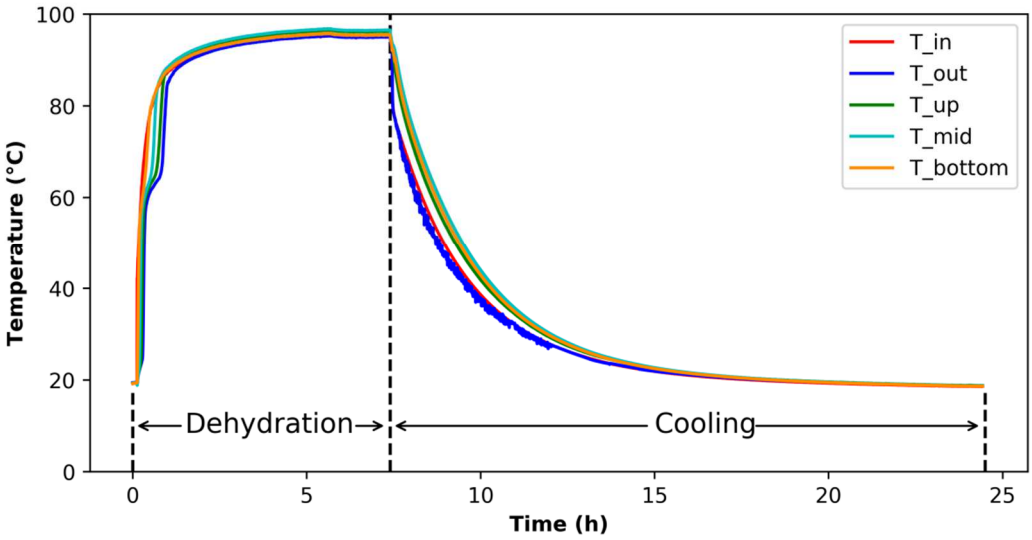

Figure 10. The temperature evolution of thermocouples in the reactor during dehydration (95.2 °C & 6.1 m^3/h) and cooling (no air circulation).

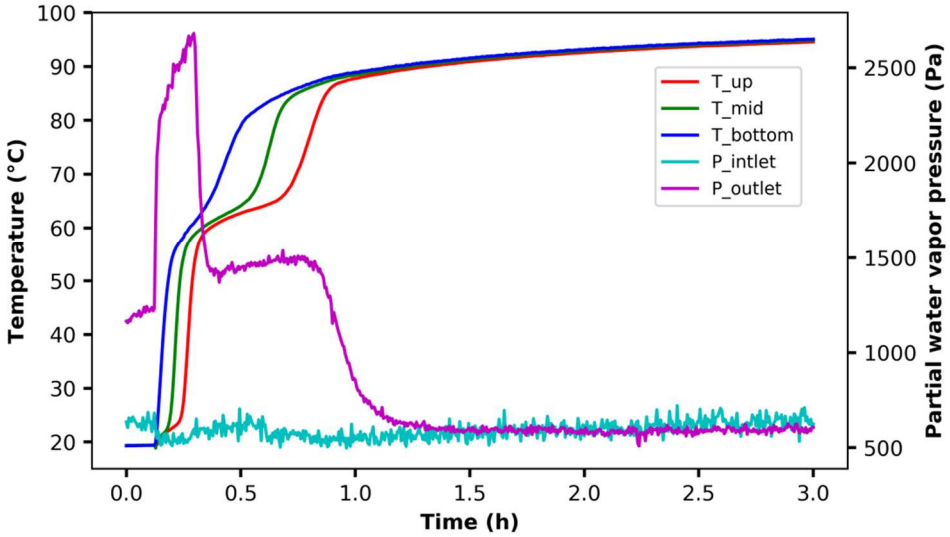

429

430 **Figure 11. The evolution of reactor temperatures and partial water vapor pressure at**

431 **outlet of system during first hours of dehydration (95.2 °C & 6.1 m^3/h).**

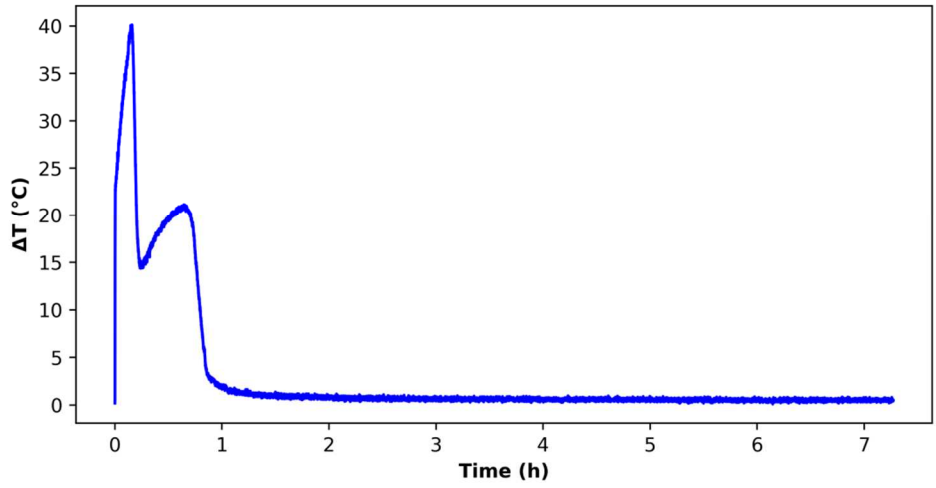

432

433 **Figure 12. The difference of temperatures at up and bottom position of fixed-bed**

434 **sample during dehydration.**

435 **Table 6. Experimental results for dehydration*.**

Final temperature (°C) at	Flow	Weight of	Weight after	Percent of

the reactor inlet	(m^3/h)	samples (g)	dehydration (g)	loss (%)
95.0 ± 0.1 (95)	7.5	74.80	49.75	33.5
95.2 ± 0.2 (95)	6.1	77.30	52.25	32.4
92.8 ± 0.2 (95)	5.1	70.25	45.90	34.7
84.1 ± 0.1 (85)	5.1	74.85	50.30	32.5
76.8 ± 0.2 (75)	5.1	79.45	54.30	31.7

*The number in the brackets is the targeted temperature of dehydration in the reactor. The incertitude of flowrate is ± 0.1 m^3/h while ± 0.05 g for weight.

3.5 Reactor tests for hydration

After the stabilization of the humid airflow psychrometric values, 20.0 °C & 90.0 % RH, the three-way valve was turned on to introduced the humid airflow into the reactor and then hydrate the material. Then, the water vapor diffused into the porosity of the material and get absorbed to release thermal energy and increase the temperature of the fixed-bed. Meanwhile, the airflow entering the reactor advected the heat produced. In this way, the stored chemical energy was transferred into the airflow in order to heat the household.

The inlet relative humidity at 20.1 °C is pre-stabilized at 90.1 % RH. According to **Eq. 3 – 5**, the PWVP is set to 2280 ± 60 Pa during the hydration phase (showed in Fig. 13a). During the hydration, the outlet PWVP decreases to 270 Pa due to very strong sorption of water vapor at the surface of materials. In the meantime, the material presents a very sharp increase in temperature above the constant inlet airflow temperature of 21.9 °C. In Fig. 13b, the bottom temperature increase is about 12.8 °C while the middle temperature and top temperature reach, respectively, 26.8 °C and 34.1 °C. This gradual evolution in different locations is the result of heat advection from the material located at the lower position in the reactor. It also leads to a time shifting of the peak visible in Fig. 13c, which shows a zoom of the first 30 minutes.

Moreover, the maximal temperature of the airflow leaving the reactor is 57.5 °C with an increase of 37.5 °C. Similarly showed in Fig. 14 for the same period, the rate of water vapor sorption is as high as 71.4 g/h by the fixed-bed, which leads to a steep rise in the quantity of water vapor absorbed.

Afterward, the PWVP at the outlet of the system increases rapidly (Fig. 13a), which corresponds to a sharp decrease in the rate of sorption. Consequently, the temperatures in the fixed-bed decrease in the following order: bottom, middle and finally up-side. The temperature of the airflow leaving the reactor decreased to 30.3 °C. Then all the temperatures decreases slowly when the water sorption rate reduces. This tail-off may be due to the low diffusion rate of water vapor in the material granules thereby the low quantity of available water resources for exothermic reaction under the operating conditions. Fig. 13b shows that the thermal energy release lasted about 2.5 hours and the water sorption rate is close to 0. However, the slight increase of water vapor absorbed could be observed but not visible in temperature during the last hour of the experiment in Fig. 13b. The profile of temperature curves and water adsorption rate could be modified, not only by improving the porosity and thermal conductivity of material itself [23], but also by low airflow rate or adding more materials to extend the duration of the temperature peaks.

a)

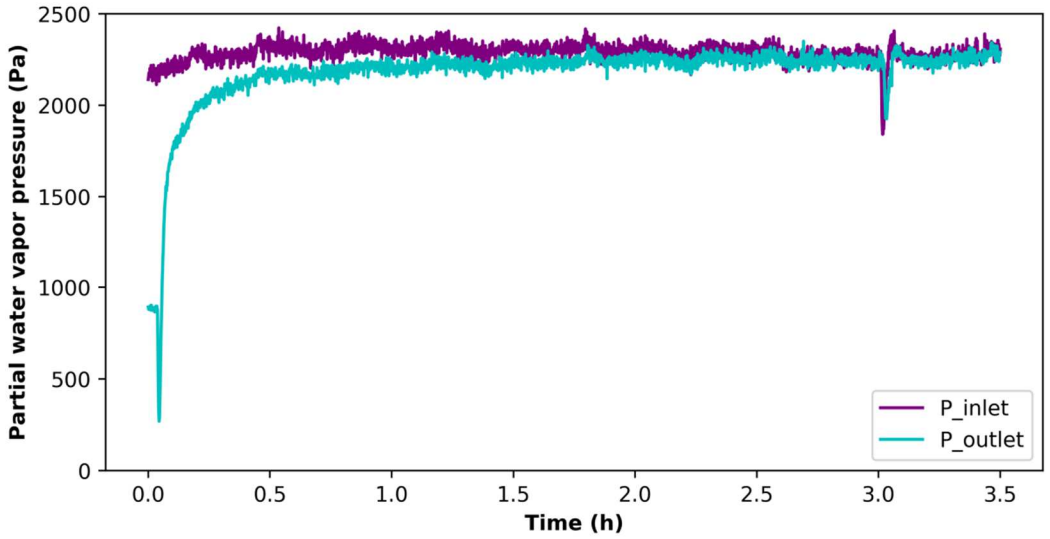
Partial water vapor pressure (Pa)
2500
2000
1500
1000
500
0
0.0
0.5
1.0
1.5
2.0
2.5
3.0
3.5
Time (h)
P_inlet
P_outlet

b)

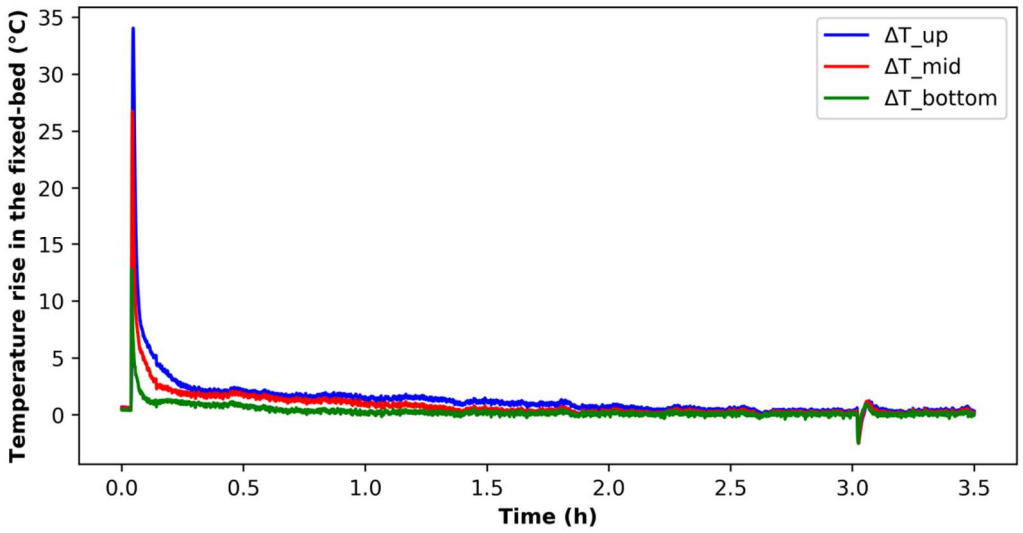
Temperature rise in the fixed-bed (°C)
35
30
25
20
15
10
5
0
0.0
0.5
1.0
1.5
2.0
2.5
3.0
3.5
Time (h)
ΔT_up
ΔT_mid
ΔT_bottom

c)

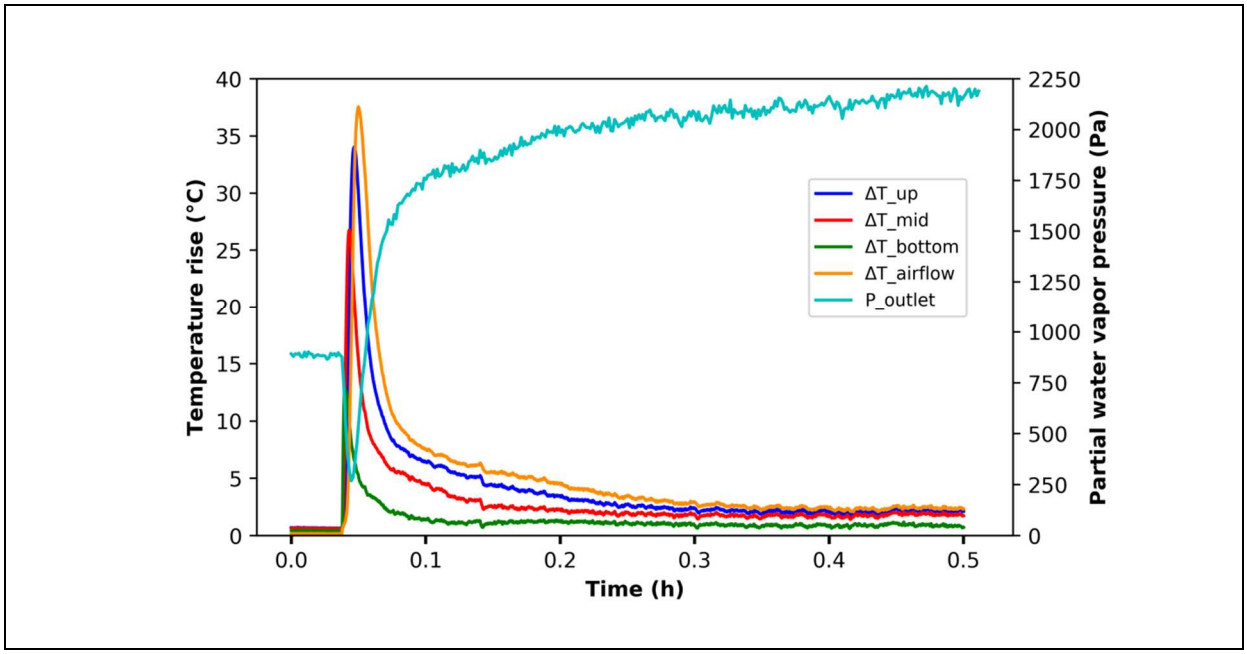

Figure 13. Hydration performance at 90.1 % RH and 20.1 °C in the reactor: a) The increase of temperatures in the fixed-bed and b) PWVP evolution and c) for the first 30 minutes.

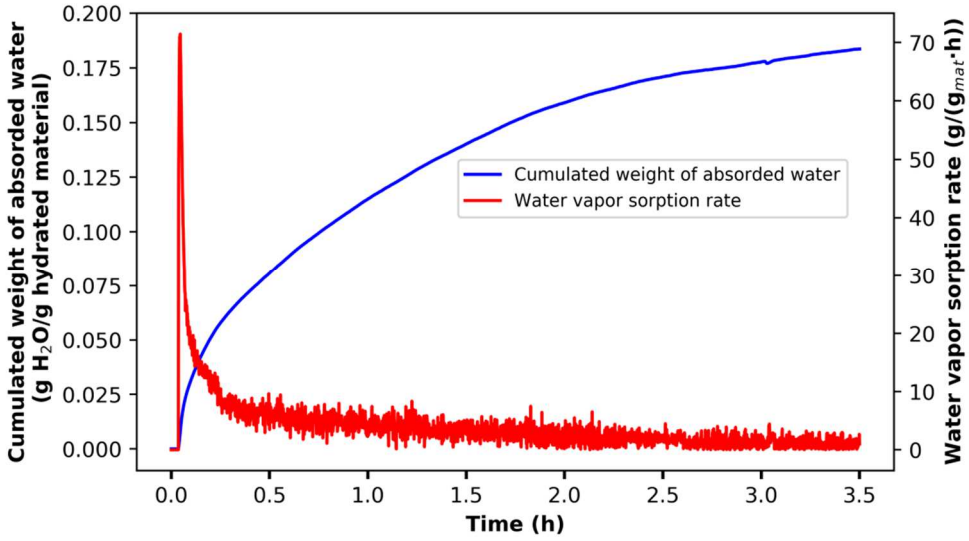

Figure 14. Kinetics of water sorption during hydration at 20.1 °C and 90.1 % RH.

As a porous material, a certain amount of water vapor could condense in the pores. Therefore, the heat released could be owed to the chemical reaction and physical adsorption. However, it is difficult to discuss the two processes dividedly. The exothermic power and

accumulated energy were calculated from the temperature rise of airflow at the exit of the reactor by **Eq. 7** & **8**. The mass-normalized power of discharging was determined as the ratio of heat-liberating power to the weight of initial hydrated cement materials loaded in the reactor. Fig. 15 shows the evolution of the specific power during the hydration. The whole profile of the curve is similar to the temperature ones. The response of the system to release heat is very rapid and increases steeply as high as 915 W/kg hydrated material, which may come from the large water molecular bonding capacity of meta-ettringite (see **Eq. 1**). Then it reduces quickly and forms a long tail-off to 0 after 2.5 hours. The total energy in this experiment contributes to about 176 kWh/m^3 hydrated cement material, or a reactor energy density of 104 kWh/m^3. Note that the experiment is stopped after 3.5 hours due to the negligible evolution of the airflow temperature. Although the power is close to zero, the heat releasing is always in process due to the slow kinetic of water absorption. With time, the final mass should be equal, or at least, close to the initial weight.

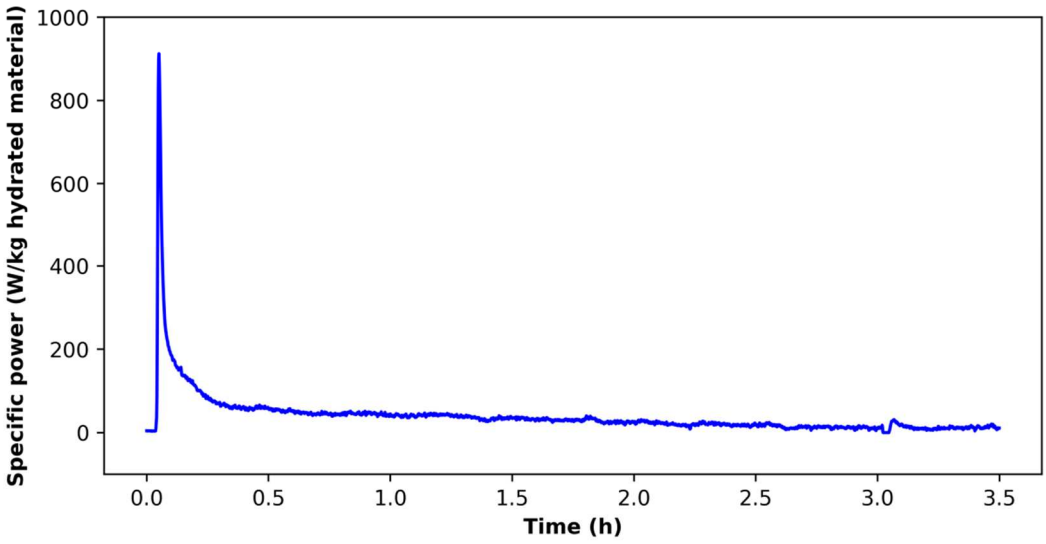

Figure 15. The hydration power of material calculated by the temperature rise of airflow exiting the reactor at 20.1 °C and 90.1 % RH.

Table 7. Results of hydration experiments under different operating conditions*.

Hydration temperature (°C)	Flow (m^3/h)	RH (%)	Weight of de-hydrated samples (g)	Percent of water gain on initial hydrated sample) (%)	T _out max. (°C)	Specific max. power (W/kg $_{initial\ hydrated\ sample}$)	Material energy density & packed bed energy density (kWh/m^3)
20.1 ± 0.2 (20)	5.1	90.1 ± 1	49.75	14.0	57.5	915	176 / 104
19.8 ± 0.2 (20)	3.1	90.2 ±1.4	53.50	10.3	59.2	630	148 / 87
20.3 ± 0.3 (20)	5.1	80.4 ±1.4	57.00	5.8	47.1	670	94 / 56
14.7 ± 0.2 (15)	5.1	92.7 ±1.2	52.25	12.9	49.1	750	175 / 103

*The number in the brackets is the targeted temperature of hydration in the reactor. The incertitude of flowrate is ± 0.1 m^3/h while ± 0.05 g for weight.

Tab. 7 summarizes the results of hydration experiments for different scenarios. The best result obtained is with the operating conditions of 20.1 °C, 5.1 m^3/h and 90.1 % RH. The reduced airflow rate could increase the temperature but decreases the maximal power due to less accessible water resources for the same period. The energy density is expected to be similar to the one with a higher airflow rate. However, the low airflow rate makes the kinetic

504 of hydration very slow, which leads to the earlier ending of the experiment. If the relative
505 humidity decreases by 10 %, the amount of water absorbed is as low as 5.8 %. Besides, a
506 lower hydration temperature may also slow down the kinetics of water vapor sorption, thereby
507 a relatively lower temperature and power. All water uptake percentages are smaller than the
508 weight loss percentages during dehydration because of the slow sorption kinetics of granules.
509 After rehydration, the granules are supposed to have a certain degree of expansion because of
510 the rehydration of ettringite crystal causing swell. Thanks to insolubility of ettringite in water,
511 this change will not lead to the over-hydration (forming a saturated solution) followed by
512 washing out of active material and agglomeration into large chunks like other salts [13] for
513 thermochemical energy storage. Besides, it should be noted that, the cyclibility of the material
514 is an important parameter to be studied if applied in real application cases.

515 ### 3.6 Comparison with other systems from the literature

516 Compared with energy storage materials issued from different authors, in **Fig. 16**, the
517 current ettringite-based material shows comparable energy storage density (excepting pure
518 salt hydrates). However, the mean releasing power of 33.3 W/kg is much higher than the other
519 energy storage materials. It is clear, from **Tab. 8**, that the maximum release power of 915
520 W/kg is much higher than the other composite materials from the literature! This significant
521 advantage comes from that ettringite can be rehydrated at very high relative humidity, which
522 enforces the hydration rate without any liquefaction of material. Besides, the high temperature
523 rise, a relatively high energy but a much lower material cost demonstrates that this ettringite-
524 based material is suitable for potential large scale use in the buildings.

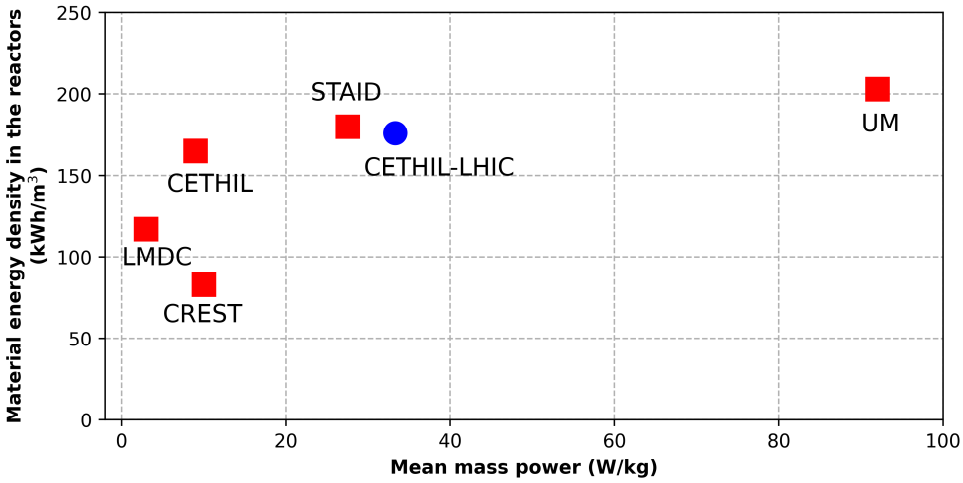

Figure 16. Comparison of thermal performances for various materials in reactor tests:LMDC (Ettringite_CSA/H_2O, [23]), CETHIL ($MgSO_4$+Zeolite 13X / H_2O, [16]), CREST (Zeolite Y-$MgSO_4$-KU20/H_2O, [34]) STAID (Zeolite 13X/H_2O, [2]) as reference, UM (Silica Gel-$SrBr_2$, [19]) and CETHIL-LHIC (Ettringite_C80P20/H_2O, in this work).

Table 8. Comparison of reactor performance for several composite thermochemical energy storage materials.

Investigations	Dehydration/hydration temperature (°C)	Hydration water vapor pressure (Pa)	Flowrate of heat-carrier (m^3/h)	Peak ΔT of heat-carrier (°C)	Maximal specific power (W/kg)	Releasing-Energy density (kWh/m^3)	References
Zeolite 13X-$MgSO_4$	150/25	2537	0.48	26	22.5	166	CETHIL [16]

Zeolite Y-$MgSO_4$-KU20/H_2O	150/20	1592	0.72	28	21.5	115	CREST [35]
Silica Gel-LiBr	150/30	1248	12.9	14.9	286	175	UM [18]
Silica Gel-$SrBr_2$	80/30	1250	12.9	/	200	230	UM [19]
Ettringite_CSA	60/20	2344	0.12	16	5.2	117	LMDC [23]
Ettringite_C80P20/H_2O	95/20	2100	5.1	37.5	915	176	CETHIL-LHIC (current work)

4 Conclusions

The present work aims at investigating the thermal performance of an ettringite-based material at micro-scale and at reactor-scale (using a new open-mode fixed-bed design). The dehydration enthalpy of material is as high as 811 J/g original hydrated materials, which equals to an energy storage density of 282 kWh/m^3. The rehydration carried out by three steps of rapid absorption, steady absorption and tailed weak absorption. The use of an open-mode reactor tests involves several operating conditions for the charging and discharging process. The dehydration temperature has a minor influence on the final mass loss due to a relatively dry ambient air supplied. Moreover, the weight loss in the reactor is higher than that in the micro-scale study because of bigger pore solution content. The dehydration temperature of ettringite in the reactor is observed at 55–65 °C. As for hydration, a higher relative humidity

543 during the discharging process can result in more released energy and a higher maximal
544 specific power. The temperature of heat-carrier could attain 57.5°C accompanied with a
545 maximal specific power of 915 W/kg during the discharging process (values that are much
546 higher than that of most energy storage composite materials). The material energy density is
547 about 176 kWh/m^3, which is very competitive with different energy storage projects. Even if
548 the present results are promising in using this kind of low-cost energy storage material for
549 short-period or seasonal thermal energy storage, the solution still needs to be developed to
550 improve the hydration kinetics by increasing its porosity or ettringite content. Furthermore,
551 large-scale prototypes are necessary before the integration into building.

552 ## 5 Acknowledgements

553 The Association Nationale de la Recherche et de la Technologie (ANRT) of France and
554 LafargeHolcim Innovation Center are greatly appreciated for the funding of this research. The
555 authors address their acknowledgment to Mr. Pascal Bost for his precise discussion and help
556 for the reactor tests.

557 ## 6 Bibliography

558 [1] Eurostat, Energy consumption in households., 2019.
559 https://ec.europa.eu/eurostat/statistics-
560 explained/index.php/Energy_consumption_in_households.

561 [2] K. Johannes, F. Kuznik, J.-L. Hubert, F. Durier, C. Obrecht, Design and
562 characterisation of a high powered energy dense zeolite thermal energy storage system
563 for buildings, Appl. Energy. 159 (2015) 80–86.
564 https://doi.org/https://doi.org/10.1016/j.apenergy.2015.08.109.

[3] E. Mastronardo, L. Bonaccorsi, Y. Kato, E. Piperopoulos, M. Lanza, C. Milone, Strategies for the enhancement of heat storage materials performances for MgO/H2O/Mg(OH)2 thermochemical storage system, Appl. Therm. Eng. 120 (2017) 626–634. https://doi.org/https://doi.org/10.1016/j.applthermaleng.2017.04.004.

[4] Y.A. Criado, M. Alonso, J.C. Abanades, Z. Anxionnaz-Minvielle, Conceptual process design of a CaO/Ca(OH)2thermochemical energy storage system using fluidized bed reactors, Appl. Therm. Eng. 73 (2014) 1087–1094. https://doi.org/10.1016/j.applthermaleng.2014.08.065.

[5] J. Yan, C.Y. Zhao, Experimental study of CaO/Ca(OH)2 in a fixed-bed reactor for thermochemical heat storage, Appl. Energy. 175 (2016) 277–284. https://doi.org/10.1016/j.apenergy.2016.05.038.

[6] M. Schmidt, M. Linder, Power generation based on the Ca(OH)2/ CaO thermochemical storage system – Experimental investigation of discharge operation modes in lab scale and corresponding conceptual process design, Appl. Energy. 203 (2017) 594–607. https://doi.org/10.1016/j.apenergy.2017.06.063.

[7] Y. Yuan, Y. Li, L. Duan, H. Liu, J. Zhao, Z. Wang, CaO/Ca(OH)2 thermochemical heat storage of carbide slag from calcium looping cycles for CO2 capture, Energy Convers. Manag. 174 (2018) 8–19. https://doi.org/10.1016/j.enconman.2018.08.021.

[8] C. Ortiz, J.M. Valverde, R. Chacartegui, L.A. Perez-Maqueda, P. Giménez, The Calcium-Looping (CaCO3/CaO) process for thermochemical energy storage in Concentrating Solar Power plants, Renew. Sustain. Energy Rev. 113 (2019) 109252. https://doi.org/https://doi.org/10.1016/j.rser.2019.109252.

587 [9] M. Wokon, T. Bauer, M. Linder, Investigations on thermochemical energy storage
588 based on manganese-iron oxide in a lab-scale reactor, AIP Conf. Proc. 1850 (2017)
589 200–214. https://doi.org/10.1063/1.4984457.

590 [10] A. Singh, S. Tescari, G. Lantin, C. Agrafiotis, M. Roeb, C. Sattler, Solar
591 thermochemical heat storage via the Co3O4/CoO looping cycle: Storage reactor
592 modelling and experimental validation, Sol. Energy. 144 (2017) 453–465.
593 https://doi.org/https://doi.org/10.1016/j.solener.2017.01.052.

594 [11] M. Neises, S. Tescari, L. de Oliveira, M. Roeb, C. Sattler, B. Wong, Solar-heated
595 rotary kiln for thermochemical energy storage, Sol. Energy. 86 (2012) 3040–3048.
596 https://doi.org/10.1016/j.solener.2012.07.012.

597 [12] H. Zondag, B. Kikkert, S. Smeding, R. de Boer, M. Bakker, Prototype thermochemical
598 heat storage with open reactor system, Appl. Energy. 109 (2013) 360–365.
599 https://doi.org/10.1016/j.apenergy.2013.01.082.

600 [13] K.E. N'Tsoukpoe, T. Schmidt, H.U. Rammelberg, B.A. Watts, W.K.L. Ruck, A
601 systematic multi-step screening of numerous salt hydrates for low temperature
602 thermochemical energy storage, Appl. Energy. 124 (2014) 1–16.
603 https://doi.org/https://doi.org/10.1016/j.apenergy.2014.02.053.

604 [14] B. Michel, N. Mazet, P. Neveu, Experimental investigation of an innovative
605 thermochemical process operating with a hydrate salt and moist air for thermal storage
606 of solar energy: Global performance, Appl. Energy. 129 (2014) 177–186.
607 https://doi.org/https://doi.org/10.1016/j.apenergy.2014.04.073.

608 [15] Y.J. Zhao, R.Z. Wang, Y.N. Zhang, N. Yu, Development of SrBr2 composite sorbents
609 for a sorption thermal energy storage system to store low-temperature heat, Energy.
610 115 (2016) 129–139. https://doi.org/10.1016/j.energy.2016.09.013.

611 [16] S. Hongois, F. Kuznik, P. Stevens, J.J. Roux, Development and characterisation of a
612 new MgSO4-zeolite composite for long-term thermal energy storage, Sol. Energy
613 Mater. Sol. Cells. 95 (2011) 1831–1837. https://doi.org/10.1016/j.solmat.2011.01.050.

614 [17] B. Chen, F. Kuznik, M. Horgnies, K. Johannes, V. Morin, E. Gengembre,
615 Physicochemical properties of ettringite/meta-ettringite for thermal energy storage:
616 Review, Sol. Energy Mater. Sol. Cells. 193 (2019) 320–334.
617 https://doi.org/https://doi.org/10.1016/j.solmat.2018.12.013.

618 [18] E. Courbon, P.D. Ans, O. Skrylnyk, M. Frère, New prominent lithium bromide-based
619 composites for thermal energy storage, J. Energy Storage. 32 (2020) 101699.
620 https://doi.org/10.1016/j.est.2020.101699.

621 [19] E. Courbon, P.D. Ans, A. Permyakova, O. Skrylnyk, N. Steunou, M. Degrez, M. Frère,
622 A new composite sorbent based on SrBr2 and silica gel for solar energy storage
623 application with high energy storage density and stability, 190 (2017) 1184–1194.
624 https://doi.org/10.1016/j.apenergy.2017.01.041.

625 [20] A. Shkatulov, R. Joosten, H. Fischer, H. Huinink, Core − Shell Encapsulation of Salt
626 Hydrates into Mesoporous Silica Shells for Thermochemical Energy Storage, (2020).
627 https://doi.org/10.1021/acsaem.0c00971.

628 [21] Y. Sun, A. Spieß, C. Jansen, A. Nuhnen, S. Gökpinar, R. Wiedey, S.-J. Ernst, C. Janiak,
629 Tunable LiCl@UiO-66 composites for water sorption-based heat transformation

630 applications, J. Mater. Chem. A. 8 (2020) 13364–13375.
631 https://doi.org/10.1039/D0TA03442H.

632 [22] L.G. Baquerizo, T. Matschei, K.L. Scrivener, Impact of water activity on the stability
633 of ettringite, Cem. Concr. Res. 79 (2016) 31–44.
634 https://doi.org/https://doi.org/10.1016/j.cemconres.2015.07.008.

635 [23] K. Ndiaye, S. Ginestet, M. Cyr, Experimental evaluation of two low temperature
636 energy storage prototypes based on innovative cementitious material, Appl. Energy.
637 217 (2018) 47–55. https://doi.org/10.1016/J.APENERGY.2018.02.136.

638 [24] J. Kaufmann, F. Winnefeld, Seasonal heat storage in calcium sulfoaluminate based
639 hardened cement pastes – experiences with different prototypes, J. Energy Storage. 25
640 (2019).

641 [25] B. Chen, Study of an ettringite-based thermochemical energy storage for buildings,
642 INSA of Lyon, 2020.

643 [26] H.F.W. Taylor, Cement chemistry, 2nd., Thomas Telford, London, 1997.

644 [27] B. Chen, M. Horgnies, B. Huet, V. Morin, K. Johannes, F. Kuznik, Comparative
645 kinetics study on carbonation of ettringite and meta-ettringite based materials, Cem.
646 Concr. Res. 137 (2020) 106209.
647 https://doi.org/https://doi.org/10.1016/j.cemconres.2020.106209.

648 [28] G. J.A., Goff; S., Low-temperature properties of water from -160° to 212 °F., Trans.
649 Am. Soc. Heat. Vent. Eng. 52 (1946) 95–121.

[29] L. Okhrimenko, L. Favergeon, K. Johannes, F. Kuznik, M. Pijolat, Thermodynamic study of MgSO4–H2O system dehydration at low pressure in view of heat storage, Thermochim. Acta. 656 (2017) 135–143. https://doi.org/10.1016/j.tca.2017.08.015.

[30] F. Kuznik, K. Johannes, Thermodynamic efficiency of water vapor/solid chemical sorption heat storage for buildings: Theoretical limits and integration considerations, Appl. Sci. 10 (2020). https://doi.org/10.3390/app10020489.

[31] A. Fick, Ueber Diffusion, Ann. Phys. 170 (1855) 59–86. https://doi.org/10.1002/andp.18551700105.

[32] X. Bian, C. Kim, G.E. Karniadakis, 111 years of Brownian motion, Soft Matter. 12 (2016) 6331–6346. https://doi.org/10.1039/C6SM01153E.

[33] Z.H. Pan, C.Y. Zhao, Gas–solid thermochemical heat storage reactors for high-temperature applications, Energy. 130 (2017) 155–173. https://doi.org/10.1016/j.energy.2017.04.102.

[34] S.Z. Xu, R.Z. Wang, L.W. Wang, J. Zhu, Performance characterizations and thermodynamic analysis of magnesium sulfate-impregnated zeolite 13X and activated alumina composite sorbents for thermal energy storage, Energy. 167 (2019) 889–901. https://doi.org/10.1016/j.energy.2018.10.200.

[35] D. Mahon, G. Claudio, P. Eames, A study of novel high performance and energy dense zeolite composite materials for domestic interseasonal thermochemical energy storage, Energy Procedia. 158 (2019) 4489–4494. https://doi.org/10.1016/j.egypro.2019.01.763.